Combined spectroscopic and *ab initio* investigation of monolayer-range Cr oxides on Fe(001): The effect of ordered vacancy superstructure

Alberto Calloni,[1,*] Guido Fratesi,[2,*] Simona Achilli,[2] Giulia Berti,[1,†] Gianlorenzo Bussetti,[1] Andrea Picone,[1] Alberto Brambilla,[1] Paola Folegati,[1] Franco Ciccacci,[1] and Lamberto Duò[1]

[1]*Dipartimento di Fisica, Politecnico di Milano, Piazza Leonardo Da Vinci 32, 20133 Milano, Italy*

[2]*ETSF and Dipartimento di Fisica, Università degli Studi di Milano, via Celoria 16, 20133 Milano, Italy*

(Received 18 February 2017; revised manuscript received 9 June 2017; published 21 August 2017)

We investigated the electronic structure of an ultrathin Cr oxide film prepared by growing about 0.8 monolayers of Cr on the oxygen-terminated Fe(001)-$p(1\times1)$O surface and characterized by the formation of an ordered array of Cr vacancies producing a $(\sqrt{5}\times\sqrt{5})R27^\circ$ superstructure. We combined experimental techniques such as angle- and spin-resolved photoemission spectroscopy, low-energy electron diffraction, and scanning tunneling spectroscopy with *ab initio* calculations, focusing on (i) the peculiar energy dispersion of O $2p$ states and (ii) the orbital and spin character of Cr $3d$ states. We show that the experimental O $2p$ dispersion can be related to the presence of an ordered vacancy lattice. The comparison with the existing literature on the oxidation of bulk Cr(001), where a network of Cr vacancies with a short-range crystallographic order is present, reveals a similar effect on O states. The valence electronic structure of the Cr oxide layer is mostly composed by spin-minority Cr states, consistent with an antiferromagnetic coupling with the Fe substrate.

DOI: 10.1103/PhysRevB.96.085427

I. INTRODUCTION

The characterization of the physicochemical properties of transition-metal oxides is one of the leading topics of current research in condensed matter physics, mainly due to their many applications, from catalysis to corrosion protection and electronics [1,2]. Thanks to their peculiar electronic structure, featuring localized d states, some of those oxides can be electrically polarized (i.e., show a ferroelectric behavior) and/or magnetized [ferromagnetic (FM) or antiferromagnetic (AF) behavior] [3,4], and are therefore investigated for magnetic data storage and spin-sensitive microelectronics, or spintronics. In order to downscale the physical dimensions of the devices, the latter applications are based on very thin films, engineered to exploit the characteristic phenomena arising at the oxide surfaces and interfaces [5]. In this framework, an important issue to be considered is the concentration of defects in the oxide layer. Randomly distributed point defects are always present in oxide compounds, in the form of either cation or oxygen vacancies (color centers). Besides these intrinsic defects, long-range ordered arrays of atomic vacancies have been recently found to develop in a number of monolayer transition-metal oxides epitaxially grown on a different metal substrate (see, e.g., Ref. [6] and references therein). These long-range ordered defects have been mainly investigated with respect to their chemical reactivity [7] or their properties to drive the self-assembly of nanoparticles [8], and it is expected that they can also heavily affect the electronic structure of the metal-oxide interface.

The influence of long-range ordered defects is of particular interest in the case of interfaces between transition-metal oxides and FM materials, because the configuration of the spin-polarized electronic states near the Fermi energy (E_F) is at the root of the spin filtering phenomenon occurring in magnetic tunneling junctions [9]. We have recently investigated such systems, with a particular focus on the coupling with the ferromagnetic Fe(001) substrate [10,11].

In the specific case of Cr oxide, for instance, we have demonstrated the feasibility of growing one-layer-thick films by Cr deposition on the oxygen-terminated Fe(001)-$p(1\times1)$O surface, exploiting the tendency of oxygen to segregate and bind to Cr atoms [12]. The result is a Cr oxide layer characterized by (i) a very sharp interface with Fe, i.e., showing little chemical mixing even at high temperatures; (ii) a Cr-$(\sqrt{5}\times\sqrt{5})R27^\circ$O superstructure [Cr-$(\sqrt{5}\times\sqrt{5})$O in the following], clearly observed with low-energy electron diffraction (LEED) and scanning tunneling microscopy (STM) [13]; and (iii) a magnetization antiparallel to that of the substrate [14,15]. The Cr-$(\sqrt{5}\times\sqrt{5})$O superstructure consists in a regular network of cation (Cr) vacancies created in an otherwise stoichiometric CrO layer [Cr-$p(1\times1)$O in the following], that is primarily due to electronic effects also responsible for the formation of cation vacancies in bulk oxides characterized by a rocksalt structure, as in the case of early $3d$ and $4d$ metal oxides [16]. While thick Cr oxides are characterized either by the corundum (Cr_2O_3) or rutile (CrO_2) structure, cubic phases such as the rocksalt (CrO) or the spinel (γ-Cr_2O_3) can be stabilized in ultrathin films [17,18].

In this paper, we provide a combined experimental and theoretical investigation of the Cr-$(\sqrt{5}\times\sqrt{5})$O surface band structure, based on *ab initio* calculations compared to angle- and spin-resolved photoemission spectroscopy (ARPES and SRPES, respectively) and scanning tunneling spectroscopy (STS) experiments. While our study primarily contributes to the characterization of the Cr oxide film and the interface with Fe, a broader impact is also expected on the general understanding of the oxidation process of Cr and on the magnetic behavior of ultrathin Cr oxides. The magnetic characterization of such oxides on bulk Cr samples or thick

*alberto.calloni@polimi.it; guido.fratesi@unimi.it

†Present address: Department of Chemical Physics, Fritz-Haber-Institut der Max-Planck-Gesellschaft, Faradayweg 4-6, 14195 Berlin, Germany.

Cr films, characterized by a spin-density-wave ground state [19,20], is particularly challenging. On the clean Cr(001) surface, for instance, this gives rise to a layerwise AF order for adjacent Cr terraces [21], resulting in a nil overall magnetization. In the following we highlight clear similarities between the electronic structure of the oxidized Cr(001) surface and that of the CrO/Fe(001) system, where the presence of Cr vacancies is explicitly taken into account, and link the presence of spin-polarized features in the experimental spectra to specific features of the oxide band structure.

II. METHODS

A. Sample preparation and spectroscopic characterization

The samples were prepared by growing a thick Fe film onto an MgO(001) crystal through molecular beam epitaxy (MBE) under ultrahigh vacuum (UHV) conditions (the base pressure in the vacuum chamber was in the low 10^{-8} Pa range). The resulting clean Fe(001) surface was then exposed to 30 L ($1\,\mathrm{L} = 1.33\times10^{-4}$ Pa · s) of pure molecular oxygen at 700 K and then flash heated at 900 K to remove the oxygen in excess of one single layer, or monolayer (ML), from the surface. This procedure leads to the formation of the well-characterized Fe(001)-$p(1\times1)$O surface in which each oxygen atom sits in a fourfold symmetrical Fe hollow site [22]. The Cr-($\sqrt{5}\times\sqrt{5}$)O superstructure was prepared by dosing about 0.8 ML of Cr on the Fe(001)-$p(1\times1)$O surface kept at about 600 K [13]. The Cr deposition rate (about 0.5 ML/min) was monitored by a quartz microbalance. LEED and STM were used to confirm the good quality of the reconstructed CrO layer. The results of our structural characterization are shown in Fig. 1, together with schematics describing the expected diffraction pattern and the actual arrangement of surface atoms. Figure 1(a) also shows, in the reciprocal space, the surface Brillouin zone (SBZ) related to the Cr-$p(1\times1)$O and the reconstructed surface (red and black squares, respectively), considering the two equivalent domains of the surface reconstruction.

STM and STS measurements were performed with home-made electrochemically etched W tips mounted on an Omicron variable temperature STM housed in a UHV chamber connected to the preparation system. STM images were acquired in constant current mode, whereas a constant tip-sample separation (open feedback loop) was maintained for STS data. Tunneling spectra were acquired at room temperature (RT). Photoemission spectroscopy was performed by exciting electrons with He I radiation ($h\nu = 21.2$ eV) and detecting them by means of a 150-mm hemispherical analyzer (from SPECS GmbH) with an angular resolution (for spin-integrated measurements) of $\pm1^\circ$. UV source satellites were always subtracted. SRPES measurements were performed by means of a micro-Mott detector, mounted at the exit side of the hemispherical analyzer [23]. Samples were magnetized *in situ* at RT by applying a pulsed magnetic field of about 100 Oe along one of the equivalent ⟨100⟩ directions of the Fe substrate, and analyzed at magnetic remanence at RT. The photoelectron polarization was evaluated following the methodology explained in Ref. [23], employing a Sherman function of 0.14. Typical full width at half maximum (FWHM) energy resolution values are 15 and 120 meV for ARPES and SRPES, respectively.

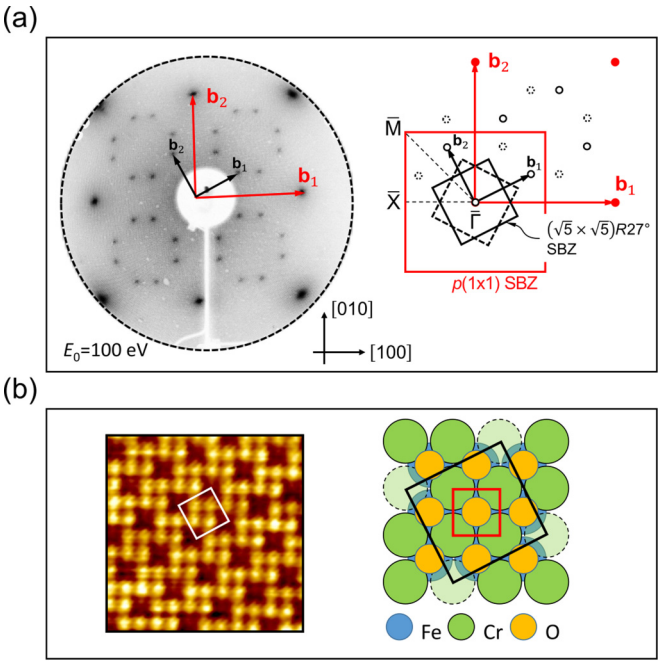

FIG. 1. (a) LEED and (b) STM images of the Cr-($\sqrt{5}\times\sqrt{5}$)O surface (the latter acquired on a 4 nm×4 nm scale, with $I = 5$ nA and $V = 100$ mV). In (a), reciprocal lattice vectors for the Cr-$p(1\times1)$O and Cr-($\sqrt{5}\times\sqrt{5}$)O surfaces are shown with red and black arrows, respectively. The related surface Brillouin zones (SBZs) are drawn as red and black squares, respectively. Two equivalent domains (continuous and dashed squares) are reported for the Cr-($\sqrt{5}\times\sqrt{5}$)O superstructure, linked by reflections with respect to either the (100) or the (010) plane. In (b) a schematic of the atomic arrangement characteristic of the Cr-($\sqrt{5}\times\sqrt{5}$)O superstructure is presented, together with the boundaries (marked with a black square) of the primitive Cr-($\sqrt{5}\times\sqrt{5}$)O cell (reproduced in the STM image with a white square in order to enhance its visibility). Cr vacancies (dashed circles) are arranged in order to form a square lattice with parameter $a' = \sqrt{5}a_{\mathrm{Fe}}$, rotated by about $\pm27^\circ$ with respect to the substrate lattice. The red square shown in the same picture identifies the primitive cell describing the $p(1\times1)$ arrangement of substrate atoms.

B. Band structure calculations

The theoretical analysis is based on first-principle density functional theory (DFT) simulations within the generalized gradient approximation for the exchange and correlation functional as proposed by Perdew, Burke, and Ernzerhof (GGA-PBE) [24], taking into account the spin polarization in a collinear description. The atomic coordinates were taken from our previous investigation on the energetic stability of surface reconstructions for monolayer-range Cr oxides grown on Fe(001) [13]. There we adopted a repeated slab model with 4 Fe(001) layers, where the bottom two are fixed at the bulk spacing. Adsorbates were placed on the other side of the slab and fully relaxed together with the two topmost Fe layers. In the present work, to better describe the surface electronic structure, we increased the slab thickness to 10 Fe(001) layers by adding at the bottom six Fe layers in bulk positions. Test

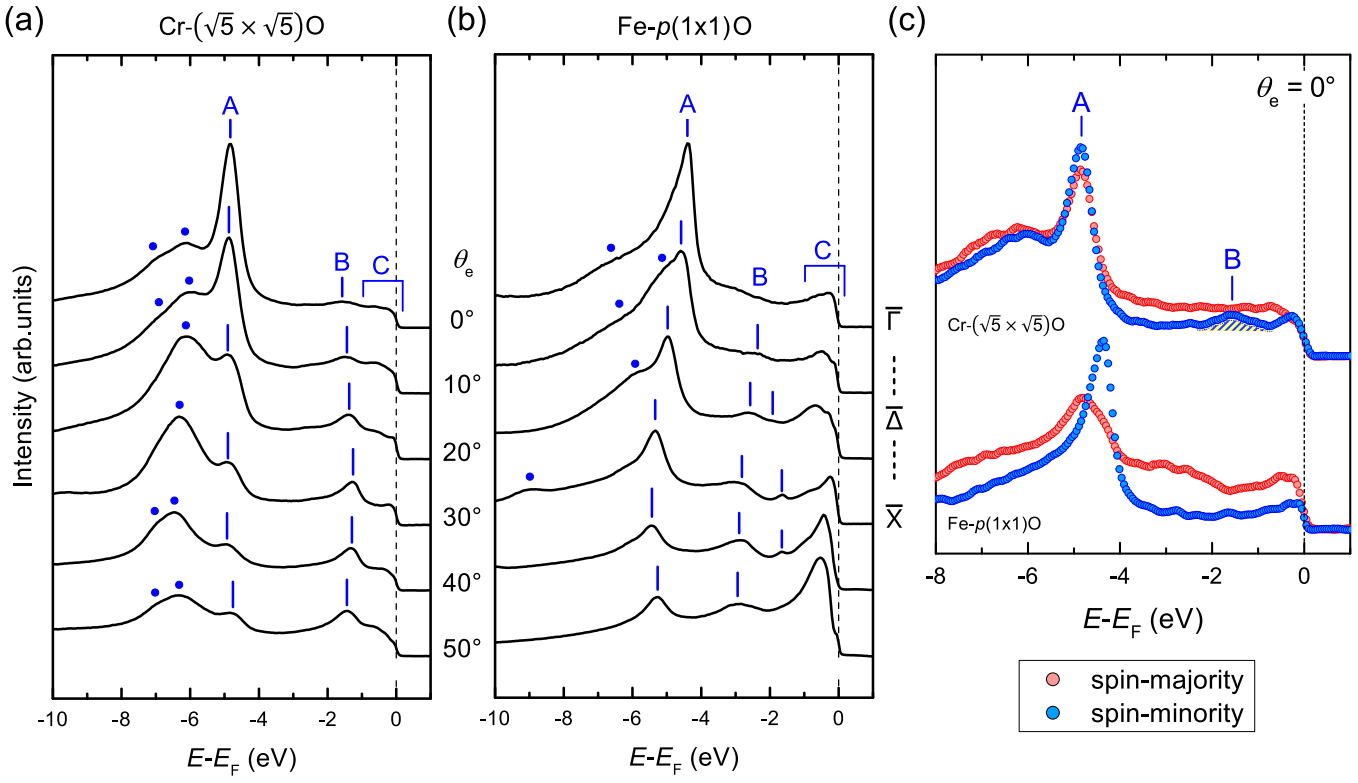

FIG. 2. Angle-resolved spectra taken from (a) the Cr-$(\sqrt{5}\times\sqrt{5})$O surface and (b) the Fe(001)-$p(1\times1)$O substrate. The spectra have been acquired at increasing polar angles (θ_e) of electron emission along the $\overline{\Gamma X}$ direction, where the $\overline{\Gamma}$ ($\overline{X}$) point is probed at $\theta_e = 0^\circ$ ($\approx 30^\circ$; see the caption of Fig. 3 for more details). Vertical lines pinpoint the position of features A and B, while minor features at larger BE are indicated by dots. The spectral region within 1 eV from the Fermi energy (E_F) is labeled C. (c) Spin-resolved spectra from the same systems. Feature B is highlighted by the hatched area.

calculations have also been run for thicker slabs (25 and 50 layers), and confirm the robustness of the presented results. A vacuum region of 12 Å separates repeated slabs from each other. The plane-wave ultrasoft pseudopotential method [25] was used as implemented in the PWSCF code of the QUANTUM-ESPRESSO distribution [26]. Other computational details can be found in Ref. [13]. To visualize the surface band structure and the contribution from the different atomic species we compute the $\boldsymbol{k}_{||}$-resolved projected density of states (KPDOS), which is defined as

$$\mathrm{KPDOS}_{\boldsymbol{R}nlm}(\boldsymbol{k}_{||}, E) = \sum_j |\langle \psi_{j\boldsymbol{k}_{||}} \mid \phi_{\boldsymbol{R}nlm}\rangle|^2 \delta(E - \varepsilon_{j\boldsymbol{k}_{||}}), \quad (1)$$

where $\phi_{\boldsymbol{R}nlm}$ is an atomic function centered at $\boldsymbol{R}$, $\psi_{j\boldsymbol{k}_{||}}$ is the eigenstate at energy $\varepsilon_{j\boldsymbol{k}_{||}}$, and the delta function is replaced by a Gaussian for plotting purposes. This allows us to effectively show surface bands also in regions where they overlap with a substrate continuum [27]. For a slab with limited thickness, artificial splitting of surface resonances in a finite number of discrete states may still be visible. The band dispersion is mapped in the reciprocal space within the first SBZ of the Fe(001) substrate [red square in Fig. 1(a) to facilitate the comparison with experiments]. We recall that the real space cell used to simulate the Cr-$(\sqrt{5}\times\sqrt{5})$O surface is about five times larger than the one required for the Cr-$p(1\times1)$O one. This, in turn, increases the number of simulated electrons and the number of bands, packed into the $(\sqrt{5}\times\sqrt{5})R27^\circ$ SBZ, by about the same amount. Finally, simulated STS are obtained by evaluating the local density of states (LDOS) in the proximity of the surface. Practically, we integrate the LDOS in a thin region extending over the full surface unit cell at a distance of 3 Å from the O atoms [28].

III. RESULTS AND DISCUSSION

A. Photoemission measurements and comparison with theoretical calculations

The photoemission spectra from the Cr-$(\sqrt{5}\times\sqrt{5})$O reconstructed surface, acquired by rotating the sample along one of the ⟨100⟩ axes, are shown in Fig. 2(a). Vertical lines highlight the position of the main photoemission features: a peak (labeled A) at a binding energy (BE) of −4.9 eV, and a broad feature (labeled B), located within the [−1.3, −1.6] eV BE interval. The position of feature B is compatible with the values reported for a similar feature observed on the oxidized Cr(001) surface at normal electron emission in Refs. [29,30]. C identifies the narrow region close to E_F.

For comparison, we have also mapped the electronic structure of a Fe(001)-$p(1\times1)$O sample in Fig. 2(b). Feature A, which in Fig. 2(a) shows practically no energy dispersion, is observed also on the oxygen-terminated Fe surface, where

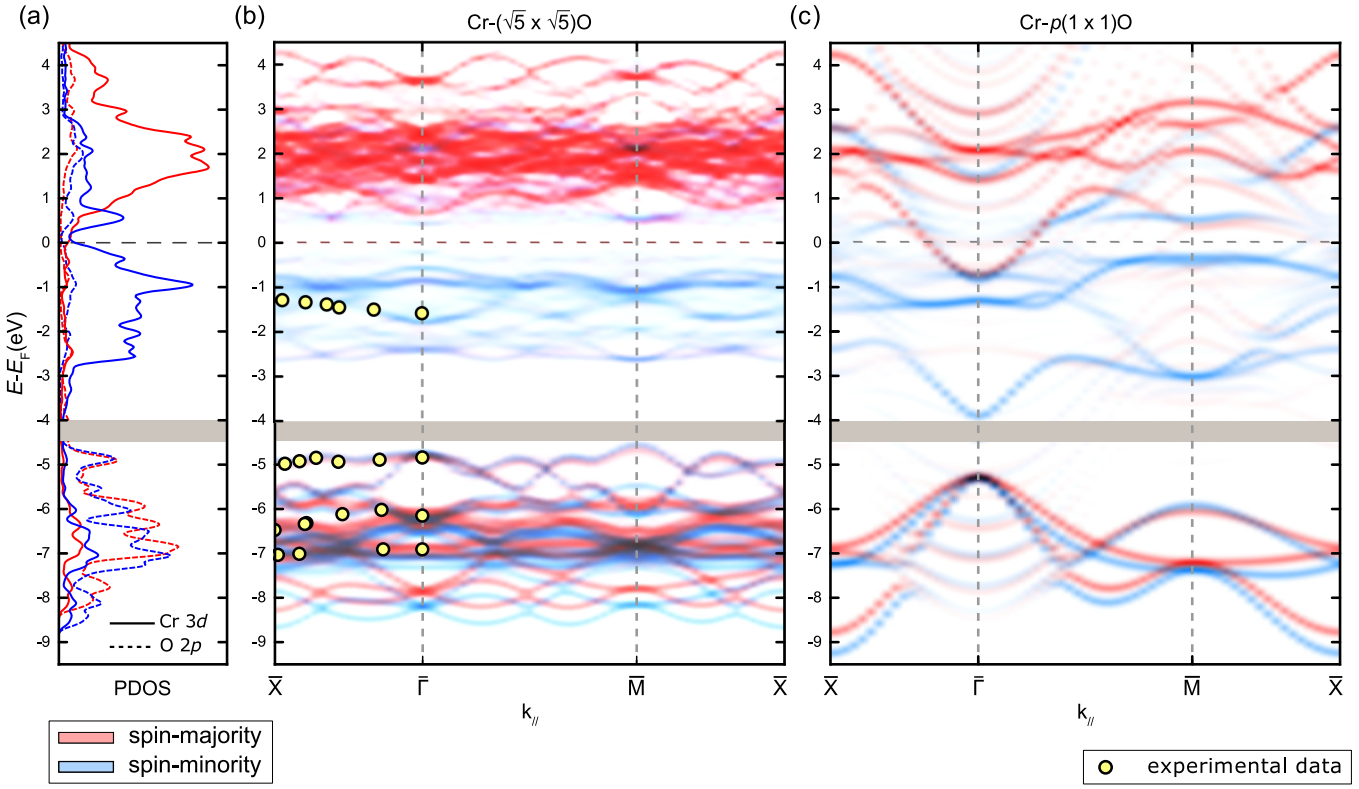

FIG. 3. For the Cr-($\sqrt{5}\times\sqrt{5}$)O surface: in (a), O- and Cr-PDOS (reported individually) integrated over the ($\sqrt{5}\times\sqrt{5}$)$R27^\circ$ SBZ; in (b), O- and Cr-KPDOS (their sum is reported) along selected high-symmetry directions of the $p(1\times1)$ SBZ; in (c), O- and Cr-KPDOS for the Cr-$p(1\times1)$O surface. The spin-majority and spin-minority populations, as defined by their occupations in the Fe substrate, are depicted in red and blue, respectively. Dots in (b) mark the BE position of the photoemission features observed on the Cr-($\sqrt{5}\times\sqrt{5}$)O surface. The photoelectron momentum in the direction parallel to the (001) surface was calculated according to Ref. [34] as $k_{||} = 0.51\ \text{Å}^{-1}\sqrt{(21.22 - |E_B| - \phi)/\text{eV}}\sin\theta_e$ with E_B being the BE and ϕ the surface work function, set to 3.6 eV [18]. As indicated by the gray area, theoretical data have been shifted by 0.5 eV to higher BE in the -4 eV to -9.5 eV range to facilitate the comparison with the experimental findings.

it clearly shifts away towards lower BE at off-normal electron emission. Closer to E_F new features appear, reminiscent of feature B in Fig. 2(a) and therefore identified with the same letter. Spin-resolved photoemission spectra, acquired at normal electron emission, are shown in Fig. 2(c). The bottom spectra, related to the Fe(001)-$p(1\times1)$O substrate, show a net majority polarization close to E_F, consistent with the available literature on Fe(001) [31,32], together with a clear splitting of feature A. In the top spectra, acquired on the Cr-($\sqrt{5}\times\sqrt{5}$)O reconstructed surface, feature B (hatched area) clearly shows a minority character, while no splitting is observed for feature A.

Good agreement is found between our results for the Fe(001)-$p(1\times1)$O substrate in Figs. 2(b) and 2(c) and the findings of the combined experimental and theoretical study of Ref. [33]. There, a primitive cell with a $p(1\times1)$ symmetry is used for the simulations, consistent with the absence of cation vacancies on the oxygen-terminated Fe surface [22]. Both the dispersion behavior and the spin splitting of feature A are nicely reproduced by the simulations. Moreover, several surface states are identified which are likely to contribute to feature B in Fig. 2(b): a majority surface resonance at -2.8 eV close to $\overline{\Gamma}$ and two surface states at -1.4 and -2.6 eV within the projected gap in the minority spin system at $\overline{X}$. The theoretical analysis of Ref. [33] allows us to assign the feature A to O $2p$ states while C and B are related to the Fe substrate. Analogously, a similar assignment is expected to hold in the case of Cr oxide surface and will be confirmed here.

In Fig. 3, the position of the photoemission features observed in the ARPES spectra from the Cr-($\sqrt{5}\times\sqrt{5}$)O surface (yellow dots), is compared with the simulated KP-DOS on O and Cr species calculated for the reconstructed system [Fig. 3(b), complemented by Fig. 3(a), showing the SBZ-integrated PDOS] and the ideal Cr-$p(1\times1)$O surface [Fig. 3(c)]. The first-principles band structures are plotted along the path in the momentum space adopted in the experiments, i.e., by considering the high-symmetry $\overline{\Gamma X}$ and $\overline{\Gamma M}$ directions of the Fe(001) substrate. We note that these directions are not coincident with the $\overline{\Gamma X}'$ and $\overline{\Gamma M}'$ directions of the two ($\sqrt{5}\times\sqrt{5}$)$R27^\circ$ SBZ shown in Fig. 1(a). However, the $\overline{\Gamma X}$ and $\overline{\Gamma M}$ lines cut the ($\sqrt{5}\times\sqrt{5}$)$R27^\circ$ SBZ along equivalent directions so that they are expected to contribute with symmetry-equivalent states to the electronic structure described both by calculations and by angle-resolved photoemission experiments.

The spin-majority and spin-minority labels in Fig. 3 refer to the occupation of the related electronic states in the Fe substrate. Examining first the PDOS [Fig. 3(a)], we see that O $2p$ states are found in a BE range 5–9 eV below E_F for

both spin populations, whereas the largest contribution from Cr orbitals is related to the spin-split 3*d* states around E_F. In particular, it is interesting to notice that the spin-majority (spin-minority) states are found mostly above (below) E_F, indicating that the Cr magnetic moment is opposite to that of the Fe atoms underneath. Indeed, both the minority character of feature B and its energy dispersion are in agreement with experimental data. Within 0.5 eV from E_F a straightforward comparison between this prediction and the outcome of our photoemission experiment on the Cr oxide film is impeded by the presence of the overlapping contributions between the Cr 3*d* states and that of the underlying Fe substrate, resulting also in a small spin polarization of the ARPES signal [Fig. 2(c)]. A similar problem, i.e., the contribution from bulk Cr states, is also encountered when comparing our simulated results with the other photoemission data from the literature on the oxidized Cr(001) surface [29,30]. More insight into the Cr 3*d* electronic structure will be given in Sec. III C by selectively comparing our photoemission data with electronic states characterized by a specific orbital character, and in Sec. III D by considering the results of our STS characterization.

Concerning the BE range of O 2*p* states we note that some characteristic features of the experimental spectra, such as the absence of any spin-dependent splitting of feature A, can also be observed in the simulated results of both Figs. 3(b) and 3(c). The simulated O 2*p* states are closer to E_F for the Cr-$(\sqrt{5}\times\sqrt{5})$O surface than for the Cr-$p(1\times1)$O due to the different stoichiometry of the CrO layer, characterized by a lower number of Cr cations per O atom and a slightly less negative O atomic charge in the Cr-$(\sqrt{5}\times\sqrt{5})$O superstructure ($-0.63e$, according to Löwdin population analysis) than in the Cr-$p(1\times1)$O case ($-0.65e$). In order to facilitate the comparison with the experiment, we have applied a rigid downward shift of about 0.5 eV to the computed O 2*p* band structure, which empirically includes the effect of self-energy corrections to the Kohn-Sham eigenvalues [6]. Similar to the present case, a downward shift of about 0.6 eV has to be applied to the simulated O 2*p* band structure for the Fe(001)-$p(1\times1)$O surface (see, e.g., Ref. [33]), in order to correctly reproduce the BE position of feature A (at normal emission) in Fig. 2(b). With the rigid shift, the computed energies of Fig. 3(b) are in excellent agreement with all the experimentally observed features. In particular, the peculiar absence of dispersion of feature A along the $\overline{\Gamma X}$ direction is correctly reproduced. Conversely, there is a strong BE variation along $\overline{\Gamma X}$ expected for O 2*p* states on the Cr-$p(1\times1)$O surface [Fig. 3(c)], clearly contrasting with our experimental results.

B. O 2*p* states

In order to analyze the effect of including the cation vacancies in the surface, giving rise to the Cr-$(\sqrt{5}\times\sqrt{5})$O reconstruction, we considered the contribution to the KPDOS (in the O states energy window) of a complete set of *p*-like atomic orbitals (p_x, p_y, and p_z, with the x, y, and z axes aligned to the [100], [010], and [001] crystallographic directions and centered on the O atoms). According to the available literature on the electronic properties of square adsorbate-induced superstructures resulting from the oxidation of bulk metallic samples [35,36], the energy dispersion of p_x and p_y states is linked to the strength of the in-plane bonds between O atoms. However, due to the lower symmetry of the metal-adsorbate system, a contribution is also made by the band structure of the underlying layers due to hybridization effects involving especially p_z orbitals. Hence, to clarify the origin of the dispersionless feature A, we performed additional calculations for freestanding CrO layers. In these simplified models, the substrate is removed while retaining the Cr and O atomic coordinates as determined for the Cr-$p(1\times1)$O or Cr-$(\sqrt{5}\times\sqrt{5})$O structures on Fe(001). Since this is meant to model the supported case, a magnetic configuration with all Cr spins parallel to each other was simulated also for the freestanding overlayer, even though the ground state of the latter could be possibly characterized by other magnetic arrangements. The resulting band structures are reported in Figs. 4(a)–4(c). In order to disentangle the effects of surface reconstruction and vacancy formation from the simple folding of the $p(1\times1)$ SBZ onto the $(\sqrt{5}\times\sqrt{5})R27^\circ$ SBZ, we also simulated the unreconstructed CrO layer in the Cr-$(\sqrt{5}\times\sqrt{5})$O unit cell [Fig. 4(b)].

Since out-of-plane (p_z) orbitals are strongly affected by hybridization with the substrate, only the contributions by those states with an in-plane p_x and p_y orbital character have been summed for the freestanding layer. Indeed, this is able to reproduce the main features in the O 2*p* energy range seen in Fig. 3. Referring to the Cr-$p(1\times1)$O band structure of Fig. 4(a) along the $\overline{\Gamma X}$ direction, the p_y orbital character is assigned to band $\overline{\Delta}_2$ (dashed line). $\overline{\Delta}_1$ bands (continuous lines) have a mixed orbital character (p_x and p_z) and show an avoided crossing about halfway along the $\overline{\Gamma X}$ direction. A similar analysis can be performed along the $\overline{\Gamma M}$ direction considering, instead of the p_x and p_y atomic orbitals, their linear combinations $p_x \pm p_y$ [36]. We therefore conclude that those bands associated with a p_x and p_y orbital character show a large dispersion in the (001) plane away from the $\overline{\Gamma}$ point. This simple picture translates to the band structure of Fig. 4(b) when folding the Cr-$p(1\times1)$O band structure on the $(\sqrt{5}\times\sqrt{5})R27^\circ$ SBZ. One notices the absence of the dispersionless feature A, that is instead nicely taken into account by the freestanding Cr-$(\sqrt{5}\times\sqrt{5})$O layer with the vacancies. In particular, a mixed p_x and p_y orbital character, with relative contributions depending on surface wave vector, is assigned to the flat band reproducing the BE position of feature A, as shown in Fig. 4(c).

The exceptional agreement we observe when comparing the band dispersion of in-plane O 2*p* states with the supported case discussed in the previous section and especially the presence of the dispersionless feature [marked with a dash-dotted line in Fig. 4(c)], only for the freestanding CrO layer featuring the Cr-$(\sqrt{5}\times\sqrt{5})$O superstructure, demonstrates that the introduction of Cr vacancies is the sole dominant effect. As this observation is independent of the nature of the underlying substrate (Fe, or nothing), it clearly becomes the fingerprint of the formation of a cation vacancy lattice with the $(\sqrt{5}\times\sqrt{5})R27^\circ$ periodicity.

Remarkably, good agreement is found between the simulated Cr-$(\sqrt{5}\times\sqrt{5})$O band structure and the experimental results of Ref. [29], related to photoemission from the oxidized

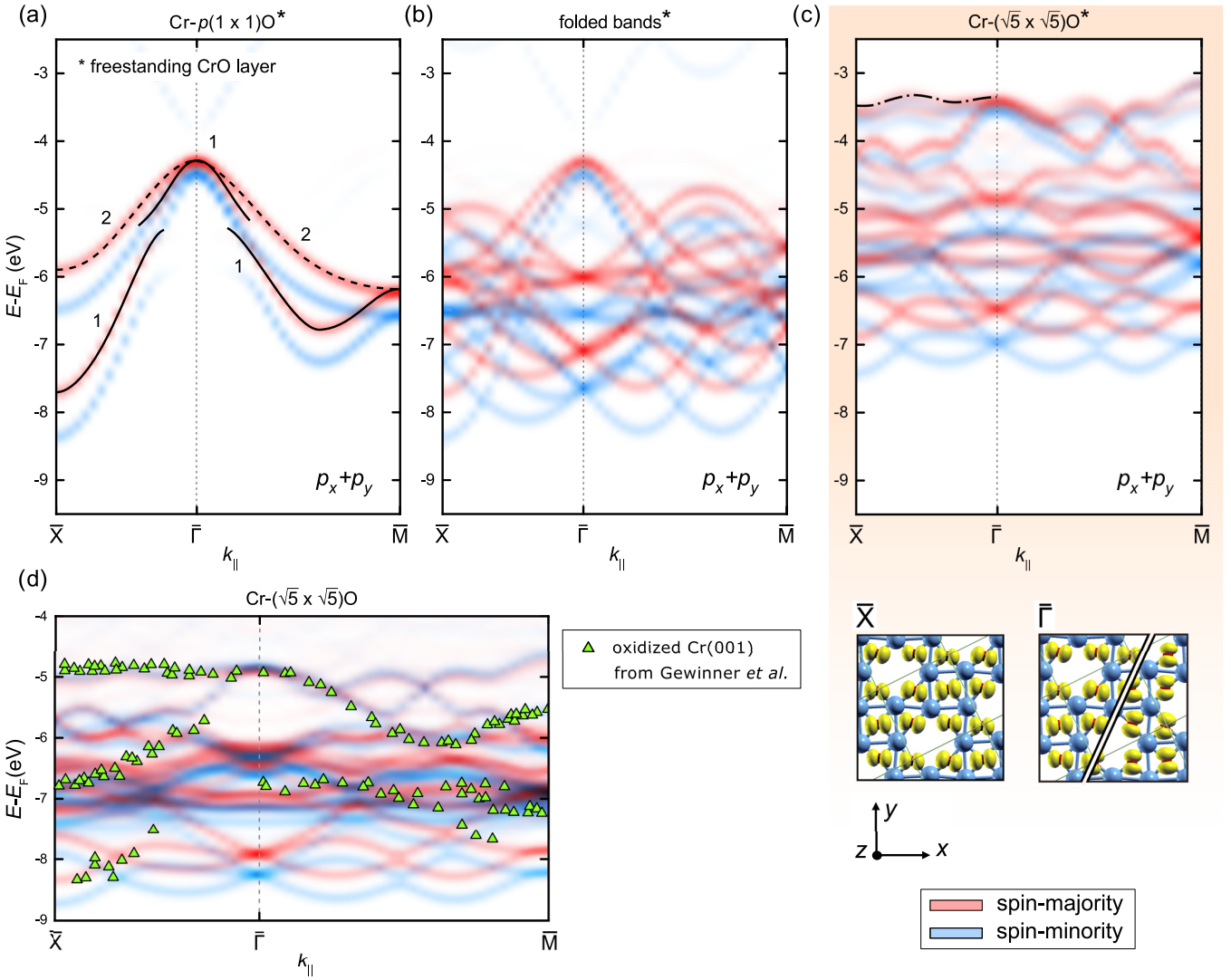

FIG. 4. (a–c) Calculated O-KPDOS along selected high-symmetry directions of the $p(1\times1)$ SBZ for a freestanding CrO layer attaining the same atomic positions as in the corresponding CrO/Fe(001) system. The simulations are presented for (a) the freestanding Cr-$p(1\times1)$O surface, (b) the same surface with the bands folded in the $(\sqrt{5}\times\sqrt{5})R27^\circ$ SBZ, and (c) the Cr-$(\sqrt{5}\times\sqrt{5})$O reconstructed surface. We note that O $2p$ states are located farther from E_F in the supported films [Figs. 3(b) and 3(c)], due to the transfer of charge there involved in the interaction with the substrate. For the Cr-$p(1\times1)$O surface, continuous (dashed) lines highlight the $\overline{\Delta}_1(\overline{\Delta}_2)$ and $\overline{\Sigma}_1(\overline{\Sigma}_2)$ states along the $\overline{\Gamma X}$ and $\overline{\Gamma M}$ directions, respectively [37] (spin-majority states are considered, for clarity). Only the states with in-plane p_x and p_y orbital character are shown. A graphical representation of the wave-function amplitude [in the form of yellow lobes, while Cr (O) atoms are drawn as blue (red) spheres] is provided in (c) for the dispersionless states highlighted with a dash-dotted line. Those states show a p_x character at $k_{||}=\overline{X}$ (left panel) and a mixed character along $\overline{\Gamma X}$, whereas two degenerate p_x and p_y states are found at $\overline{\Gamma}$ (right panel). A similar wave-function amplitude characterizes the nondispersing bands in the Cr-$(\sqrt{5}\times\sqrt{5})$O layer supported on Fe(001). (d) Comparison between the simulated O $2p$ band structure for the supported Cr-$(\sqrt{5}\times\sqrt{5})$O layer [as shown in Fig. 3(b)] and the experimental results of Ref. [29] (green triangles), related to the oxide layer produced by dosing 1 ML of oxygen on the (001) surface of bulk Cr.

Cr(001) surface. The literature data, shown in Fig. 4(d) with green triangles, are characterized by a dispersionless feature along $\overline{\Gamma X}$ at the same BE of feature A in Figs. 2(a) and 3(b). Although the authors of Ref. [29] observed only a $p(1\times1)$ pattern with LEED, local probes (such as STM) demonstrated that also the oxidized Cr(001) surface is characterized by the formation of a locally ordered cation vacancy lattice [38], sharing the same atomic arrangement of the Cr-$(\sqrt{5}\times\sqrt{5})$O superstructure. We therefore make a conclusion about a direct influence of the local ordering of surface atoms on the electronic structure investigated by means of photoemission techniques.

C. Cr 3*d* states

Following the same strategy put forth in the previous section, Fig. 5 shows the simulated Cr $3d$ band structure for the Cr-$(\sqrt{5}\times\sqrt{5})$O superstructure (left subpanels) and the Cr-$p(1\times1)$O surface (right subpanels). No energy shift is applied.

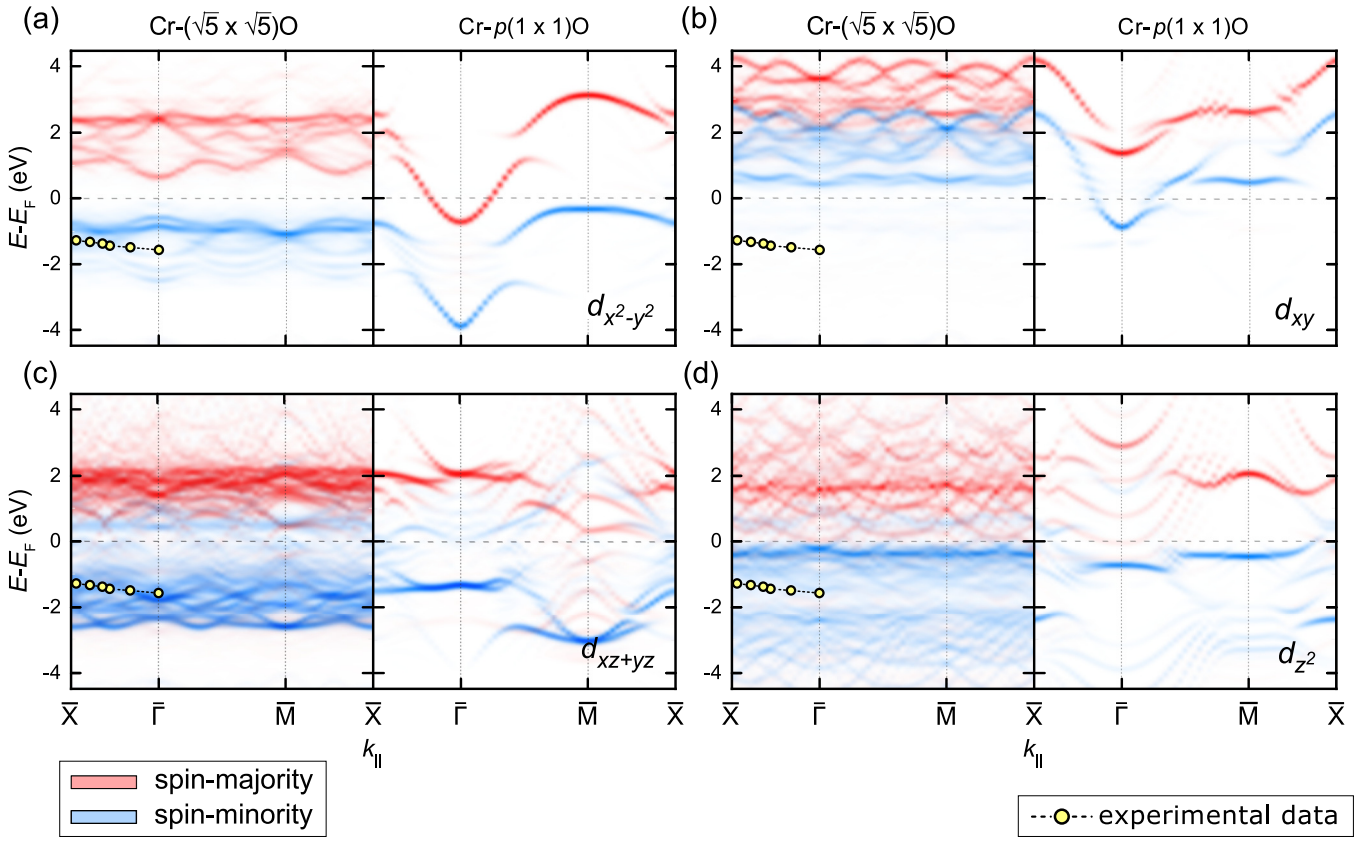

FIG. 5. Calculated band dispersion (KPDOS for Cr atoms) along selected high-symmetry directions of the $p(1\times1)$ SBZ for the Cr-$(\sqrt{5}\times\sqrt{5})$O surface (left subpanels) and the Cr-$p(1\times1)$O surface (right subpanels). Cr states are displayed according to their orbital character: (a) $d_{x^2\text{-}y^2}$, (b) d_{xy}, (c) d_{xz+yz}, and (d) d_{z^2}. Yellow dots mark the energy dispersion along $\overline{\Gamma}\overline{\mathrm{X}}$ of the photoemission feature B observed in Fig. 2(a) (see the caption of Fig. 3 for more details).

In both cases, the splitting between the majority and minority band structures is large, so that the filled Cr electronic states mainly retain a minority character. Similar to the O $2p$ case, a better understanding of the effects of the different surface geometries is achieved by considering the orbital composition of the electronic states. The $d_{x^2\text{-}y^2}$ and d_{xy} states [Figs. 5(a) and 5(b)] exhibit the largest dispersion among the $3d$ states for the Cr-$p(1\times1)$O surface, leading even to the partial filling of majority states in a narrow region close to the $\overline{\Gamma}$ point. The minority $d_{x^2\text{-}y^2}$ band extends from -4 eV up to E_F forming a plateau around the $\overline{\mathrm{M}}$ point of the SBZ. Those states are related to $3d$ orbitals connecting nearest-neighbor Cr atoms along the [100] and [010] directions in the (001) plane. They have an antibonding character at the zone boundary, so that their filling upon O exposure produces a destabilization of the CrO overlayer, which eases the formation of vacancies, as earlier discussed in Ref. [16] for the oxidation of the (001) surface of bulk Cr. The removal of Cr atoms clearly affects the in-plane delocalization of such states and the BE difference between the bonding and antibonding configurations, eventually resulting in a lower BE of the antibonding states. A similar behavior is observed for the d_{xy} states [Fig. 5(b)] which, in addition, are lifted above E_F by the introduction of the vacancies. Taking into account that d_{xy} states point towards the [110] and [1$\bar{1}$0] directions, the latter observation can be explained by the larger transfer of electronic charge towards the O anions. The main changes reported for d_{xz+yz} and d_{z^2} states [Figs. 5(c) and 5(d)] can instead be explained by band folding effects. Considering the dipole selection rules associated with photoemission from the bcc (001) surface [39], no contribution is expected at normal emission from in-plane states; i.e., it is reasonable to assign either a d_{xz+yz} or d_{z^2} orbital character to feature B. In addition, the best agreement between energy position of peak B [yellow dots in Fig. 5(c)] and the calculated band structure is obtained within the BE range of d_{xz+yz} states.

D. STS data and simulations

STS results related to the Cr-$(\sqrt{5}\times\sqrt{5})$O surface are shown in Fig. 6(a), while Fig. 6(b) presents the simulated spectra obtained by evaluating the LDOS at 3 Å above the O layer in order to take into account the natural decay of the wave function outside the surface.

Below E_F, the experimental spectrum is characterized by a broad feature, composed by a peak at a BE of -0.75 eV and a shoulder at about -0.2 eV. A dip is observed at E_F. Above E_F, a 0.7-eV-wide plateau is present, followed by a steep rise starting at about 1 eV. These results nicely compare with the spin-resolved LDOS of Fig. 6(b). We can thus relate the features observed below E_F mostly to the tunneling of electrons from minority-spin states, while the plateau above E_F is mainly related to the presence of majority-spin empty states.

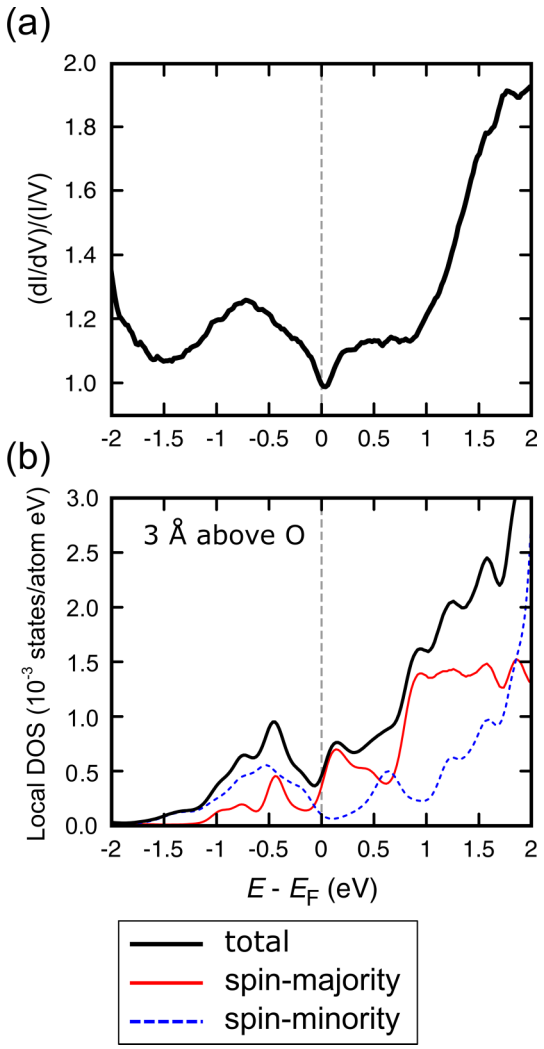

FIG. 6. (a) STS data acquired on the Cr-($\sqrt{5}\times\sqrt{5}$)O surface. The experimental spectrum has been normalized to the sample-to-tip conductance in order to account for the voltage-dependent transmission through the tunneling barrier [40]. The spectrum has to be considered as an average over the entire reconstructed surface. (b) Simulated spectra obtained from the LDOS 3 Å above the O layer.

A detailed analysis of the contributions to the simulated LDOS from various paths in the SBZ and their direct comparison with the Cr-KPDOS reported in Fig. 5 allows us to determine the dominant orbital character in the atomic regions of the states contributing to the experimental spectrum. The main contribution to the STS signal comes from d_{z^2} states [Fig. 5(d)] that display, below E_F, spin-minority flat bands in the same BE interval of the two features observed with STS, together with a smaller spin-majority contribution, and spin-majority bands just above E_F. A smaller contribution to the peak at -0.75 eV is found also from minority $d_{x^2-y^2}$ states [Fig. 5(a)]. Minority states having d_{xy} [Fig. 5(b)] and d_{xz+yz} character [Fig. 5(c)] are found to contribute to the plateau above E_F by producing a peak at about 0.6 eV.

IV. CONCLUSIONS

We have investigated the influence of an ordered lattice of Cr vacancies on the electronic structure of an ultrathin Cr oxide layer prepared by depositing 0.8 ML of Cr on a Fe(001)-$p(1\times1)$O substrate, resulting in the formation of a Cr-($\sqrt{5}\times\sqrt{5}$)O superstructure. We observe, both in the measurements and in the simulations, a prominent feature at a BE of about -5 eV characterized by a negligible energy dispersion along the $\overline{\Gamma X}$ direction of the Fe SBZ, whose origin is tracked down to the O $2p$ states. Given that this dispersionless behavior is not experimentally observed on the bare (i.e., with no Cr atoms) O-terminated substrate and it is not reproduced by our simulations for the Cr-$p(1\times1)$O surface, we conclude it is the fingerprint of the formation of Cr vacancies. In good agreement with our angle- and spin-resolved photoemission characterization, where a minority feature is clearly detected at a BE of -1.6 eV, the calculated Cr $3d$ band structure is dominated by minority states. Major changes are predicted for in-plane Cr $3d$ states, whose energy dispersion is significantly altered by the introduction of a Cr vacancy lattice.

Our results are also compared with existing literature investigations related to the early stages of the Cr(001) surface oxidation, where a similar superstructure, showing a much worse degree of crystallographic order, has been detected for O coverages close to 1 ML. A good correspondence is found, especially regarding the energy dispersion of O $2p$ states, suggesting that even for bulk Cr, the presence of vacancies should be taken into account in order to reach an accurate description of the surface electronic properties. Finally, we have performed a characterization of the states near the Fermi energy by means of STS spectroscopy. The comparison with the simulated spectrum allows a complete characterization of the features observed in the experiment.

ACKNOWLEDGMENT

The authors would like to thank M. Finazzi and F. Bottegoni for fruitful discussions.

[1] V. E. Henrich and P. A. Cox, *The Surface Science of Metal Oxides* (Cambridge University Press, Cambridge, UK, 1996).
[2] A. Clark, Oxides of the transition metals as catalysts, Ind. Eng. Chem. **45**, 1476 (1953).
[3] S.-W. Cheong, Transition metal oxides: The exciting world of orbitals, Nat. Mater. **6**, 927 (2007).
[4] *Magnetic Properties of Antiferromagnetic Oxide Materials: Surfaces, Interfaces, and Thin Films*, edited by L. Duò, M. Finazzi, and F. Ciccacci (John Wiley & Sons, Weinheim, 2010).
[5] *Oxide Ultrathin Films*, edited by G. Pacchioni and S. Valeri (Wiley-VCH, Weinheim, 2011).
[6] S. Surnev, A. Fortunelli, and F. P. Netzer, Structure–property relationship and chemical aspects of oxide–metal hybrid nanostructures, Chem. Rev. **113**, 4314 (2013).
[7] A. M. Ferrari and C. Pisani, Reactivity of the non stoichiometric Ni_3O_4 phase supported at the Pd(100) surface: Interaction with Au and other transition metal atoms, Phys. Chem. Chem. Phys. **10**, 1463 (2008).

[8] L. Gavioli, E. Cavaliere, S. Agnoli, G. Barcaro, A. Fortunelli, and G. Granozzi, Template-assisted assembly of transition metal nanoparticles on oxide ultrathin films, Prog. Surf. Sci. **86**, 59 (2011).

[9] J. Mathon and A. Umerski, Theory of tunneling magnetoresistance of an epitaxial Fe/MgO/Fe(001) junction, Phys. Rev. B **63**, 220403 (2001).

[10] M. Finazzi, L. Duò, and F. Ciccacci, Magnetic properties of interfaces and multilayers based on thin antiferromagnetic oxide films, Surf. Sci. Rep. **64**, 139 (2009).

[11] A. Picone, M. Riva, A. Brambilla, A. Calloni, G. Bussetti, M. Finazzi, F. Ciccacci, and L. Duò, Reactive metal–oxide interfaces: A microscopic view, Surf. Sci. Rep. **71**, 32 (2016).

[12] A. Calloni, A. Picone, A. Brambilla, M. Finazzi, L. Duò, and F. Ciccacci, Effects of temperature on the oxygen aided Cr growth on Fe(001), Surf. Sci. **605**, 2092 (2011).

[13] A. Picone, G. Fratesi, M. Riva, G. Bussetti, A. Calloni, A. Brambilla, M. I. Trioni, L. Duò, F. Ciccacci, and M. Finazzi, Self-organized chromium oxide monolayers on Fe(001), Phys. Rev. B **87**, 085403 (2013).

[14] A. Brambilla, G. Berti, A. Calloni, A. Picone, M. Riva, G. Bussetti, S. Nappini, E. Magnano, M. Finazzi, L. Duò, and F. Ciccacci, Magnetic properties of monolayer range chromium oxides on Fe(001), J. Appl. Phys. **114**, 123905 (2013).

[15] G. Berti, A. Brambilla, A. Calloni, G. Bussetti, M. Finazzi, L. Duò, and F. Ciccacci, Oxygen-induced immediate onset of the antiferromagnetic stacking in thin Cr films on Fe(001), Appl. Phys. Lett. **106**, 162408 (2015).

[16] A. Eichler and J. Hafner, Adsorbate-induced vacancy formation and substrate relaxation on Cr(100), Phys. Rev. B **62**, 5163 (2000).

[17] L. Zhang, M. Kuhn, and U. Diebold, Growth, structure and thermal properties of chromium oxide films on Pt(111), Surf. Sci. **375**, 1 (1997).

[18] A. Calloni, G. Berti, A. Brambilla, M. Riva, A. Picone, G. Bussetti, M. Finazzi, F. Ciccacci, and L. Duò, Electron spectroscopy investigation of the oxidation of ultra-thin films of Ni and Cr on Fe(001), J. Phys.: Condens. Matter **26**, 445001 (2014).

[19] E. Fawcett, Spin-density-wave antiferromagnetism in chromium, Rev. Mod. Phys. **60**, 209 (1988).

[20] E. Rotenberg, B. K. Freelon, H. Koh, A. Bostwick, K. Rossnagel, A. Schmid, and S. D. Kevan, Electron states and the spin density wave phase diagram in Cr(110) films, New J. Phys. **7**, 114 (2005).

[21] M. Kleiber, M. Bode, R. Ravlić, and R. Wiesendanger, Topology-Induced Spin Frustrations at the Cr(001) Surface Studied by Spin-Polarized Scanning Tunneling Spectroscopy, Phys. Rev. Lett. **85**, 4606 (2000).

[22] A. Picone, G. Fratesi, A. Brambilla, P. Sessi, F. Donati, S. Achilli, L. Maini, M. I. Trioni, C. S. Casari, M. Passoni, A. Li Bassi, M. Finazzi, L. Duò, and F. Ciccacci, Atomic corrugation in scanning tunneling microscopy images of the Fe(001)-$p(1\times1)$O surface, Phys. Rev. B **81**, 115450 (2010).

[23] G. Berti, A. Calloni, A. Brambilla, G. Bussetti, L. Duò, and F. Ciccacci, Direct observation of spin-resolved full and empty electron states in ferromagnetic surfaces, Rev. Sci. Instrum. **85**, 073901 (2014).

[24] J. P. Perdew, K. Burke, and M. Ernzerhof, Generalized Gradient Approximation Made Simple, Phys. Rev. Lett. **77**, 3865 (1996).

[25] D. Vanderbilt, Soft self-consistent pseudopotentials in a generalized eigenvalue formalism, Phys. Rev. B **41**, 7892 (1990).

[26] P. Giannozzi, S. Baroni, N. Bonini, M. Calandra, R. Car, C. Cavazzoni, D. Ceresoli, G. L. Chiarotti, M. Cococcioni, I. Dabo, A. Dal Corso, S. de Gironcoli, S. Fabris, G. Fratesi, R. Gebauer, U. Gerstmann, C. Gougoussis, A. Kokalj, M. Lazzeri, L. Martin-Samos *et al.*, QUANTUM ESPRESSO: A modular and open-source software project for quantum simulations of materials, J. Phys.: Condens. Matter **21**, 395502 (2009).

[27] G. P. Brivio, G. Butti, S. Caravati, G. Fratesi, and M. I. Trioni, Theoretical approaches in adsorption: Alkali adatom investigations, J. Phys.: Condens. Matter **19**, 305005 (2007).

[28] F. Donati, G. Fratesi, M. Passoni, C. S. Casari, A. Mairov, C. E. Bottani, M. I. Trioni, and A. Li Bassi, Strain effect on local electronic properties of Fe nanoislands grown on Au(111), Phys. Rev. B **83**, 153404 (2011).

[29] G. Gewinner, J. C. Peruchetti, and A. Jaéglé, Ordered oxygen overlayers on Cr(100) observed by LEED and photoemission, Surf. Sci. **122**, 383 (1982).

[30] H. Nakajima, S. Pukird, W. Boonyaratgalin, T. Ishii, T. Saitoh, and A. Kakizaki, Electronic and magnetic structures in O/Cr(001) surface from angle-resolved photoemission spectroscopy, J. Phys. Soc. Jpn. **79**, 104710 (2010).

[31] E. Kisker, K. Schröder, W. Gudat, and M. Campagna, Spin-polarized angle-resolved photoemission study of the electronic structure of Fe(100) as a function of temperature, Phys. Rev. B **31**, 329 (1985).

[32] L. Plucinski, Y. Zhao, C. M. Schneider, B. Sinkovic, and E. Vescovo, Surface electronic structure of ferromagnetic Fe(001), Phys. Rev. B **80**, 184430 (2009).

[33] A. Clarke, N. B. Brookes, P. D. Johnson, M. Weinert, B. Sinković, and N. V. Smith, Spin-polarized photoemission studies of the adsorption of O and S on Fe(001), Phys. Rev. B **41**, 9659 (1990).

[34] F. J. Himpsel, Experimental determination of bulk energy band dispersions, Appl. Opt. **19**, 3964 (1980).

[35] A. Liebsch, Electronic structure of $c(2\times2)$ oxygen chemisorbed on Ni(001), Phys. Rev. B **17**, 1653 (1978).

[36] G. Panzner, D. R. Mueller, and T. N. Rhodin, Angle-resolved photoemission studies of oxygen adsorbed on Fe(100), Phys. Rev. B **32**, 3472 (1985).

[37] H. Krakauer, M. Posternak, A. J. Freeman, and D. D. Koelling, Initial oxidation of the Al(001) surface: Self-consistent electronic structure of clean Al(001) and Al(001)-$p(1\times1)$O, Phys. Rev. B **23**, 3859 (1981).

[38] M. Schmid, G. Leonardelli, M. Sporn, E. Platzgummer, W. Hebenstreit, M. Pinczolits, and P. Varga, Oxygen-Induced Vacancy Formation on a Metal Surface, Phys. Rev. Lett. **82**, 355 (1999).

[39] J. Hermanson, Final-state symmetry and polarization effects in angle-resolved photoemission spectroscopy, Solid State Commun. **88**, 1097 (1993).

[40] R. M. Tromp, Spectroscopy with the scanning tunnelling microscope: a critical review, J. Phys.: Condens. Matter **1**, 10211 (1989).